

Millimeter Wave Wireless Assisted Robot Navigation with Link State Classification

Mingsheng Yin^a, Akshaj Kumar Veldanda^a, Ameer Trivedi^b, Jeff Zhang^c, Kai Pfeiffer^a, Yaqi Hu^a,
Siddharth Garg^a, Elza Erkip^a, Ludovic Righetti^a, Sundeeep Rangan^a

^aNYU Tandon School of Engineering, Brooklyn, NY, USA

^bUniversity of British Columbia, Vancouver, BC, Canada

^cHarvard University, Cambridge, MA, USA

Abstract—The millimeter wave (mmWave) bands have attracted considerable attention for high precision localization applications due to the ability to capture high angular and temporal resolution measurements. This paper explores mmWave-based positioning for a target localization problem where a fixed target broadcasts mmWave signals and a mobile robotic agent attempts to capture the signals to locate and navigate to the target. A three-stage procedure is proposed: First, the mobile agent uses tensor decomposition methods to detect the multipath channel components and estimate their parameters. Second, a machine-learning trained classifier is then used to predict the *link state*, meaning if the strongest path is line-of-sight (LOS) or non-LOS (NLOS). For the NLOS case, the link state predictor also determines if the strongest path arrived via one or more reflections. Third, based on the link state, the agent either follows the estimated angles or uses computer vision or other sensor to explore and map the environment. The method is demonstrated on a large dataset of indoor environments supplemented with ray tracing to simulate the wireless propagation. The path estimation and link state classification are also integrated into a state-of-the-art neural simultaneous localization and mapping (SLAM) module to augment camera and LIDAR-based navigation. It is shown that the link state classifier can successfully generalize to completely new environments outside the training set. In addition, the neural-SLAM module with the wireless path estimation and link state classifier provides rapid navigation to the target, close to a baseline that knows the target location.

Index Terms—Millimeter wave; positioning; SLAM; robotics; navigation; 5G

I. INTRODUCTION

THE millimeter wave (mmWave) bands have tremendous potential for new localization technologies [1]–[3] and have emerged as a central component of the positioning methods in the 3GPP Fifth Generation New Radio (5G NR) standard [4]–[8]. The wide bandwidths in the mmWave frequencies coupled with arrays with large number of elements enable detecting paths with very high delay and angular resolution.

This work considers mmWave-based positioning in the context of a robotic target localization application motivated by search and rescue applications (illustrated in Fig. 1): In this problem, a fixed target is located at some unknown position and a mobile robotic agent must locate and navigate to the

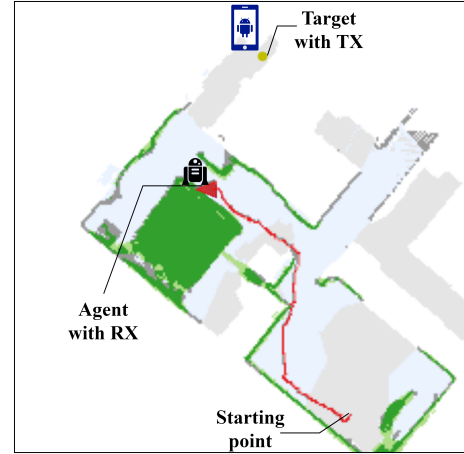


Fig. 1. **Target localization and navigation:** A target with a wireless transponder and a robotic agent must locate and navigate to the target using received wireless signals. The path and map shown in the figure are example outputs of the Active Neural-SLAM module [11] augmented with the proposed mmWave wireless path estimation and link state classification algorithm.

target in the shortest possible time. We assume the environment and obstacles are not known, so the agent also needs to map and localize itself within the environment as part of the target discovery. To assist in the target localization, the target is equipped with a mmWave transmitter that can periodically broadcast known positioning signals. The agent is equipped with a mmWave receiver that can attempt to locate the target from measurements of the positioning signals. Specifically, the agent can attempt to estimate the angles of arrivals of the signals to determine the direction in which to navigate so as to reach the target. Note that, while ultra-wide band (UWB) localization systems in traditional frequencies such as [9], [10] can achieve high temporal resolution, mmWave is uniquely able to obtain high angular resolution from a single receiver. As we will see, this angular information is critical for the target localization.

A key challenge in using angle of arrival estimation in such navigation applications is that the strongest signal may not arrive from a line-of-sight (LOS) path. In the mmWave bands in particular, signals are highly susceptible to blocking [12], [13]. As such, strongest paths often arrive via non-LOS (NLOS) routes that might involve one or more reflections or diffractions. Following paths that involve many reflec-

The authors were supported by NSF grants 1952180, 1925079, 1564142, 1547332, the SRC, OPPO, and the industrial affiliates of NYU WIRELESS. The work was also supported by RemCom that provided the Wireless Insite software.

tions/diffractions might not lead to the shortest route to the target. To use the angular information, it is thus vital to first perform some form of *link state classification* to estimate which measurements are in a LOS or NLOS state [14]–[16]. While there is a large body of work in mmWave positioning [17]–[19], link state classification in these frequencies is less understood. Positioning measurements in the mmWave range have several unique features including the need to support directional antenna elements, multiple arrays, and beam sweeping which provide more complex set of inputs for link classification. The broad goal of this work is to understand how to develop good path estimation and link state classification algorithms that can be applied in the context of target localization and navigation for realistic mmWave front-ends and signaling.

For this link state classification and target localization problem, we propose a three-step procedure: First, at each agent location, we use a modification of a low-rank tensor decomposition algorithm [20], [21] to detect signal paths and estimate their path parameters such as the angles of arrival. Second, we train a neural network to determine if the strongest path is LOS or NLOS from the path parameters. For NLOS paths, the network also determines if the path has arisen from a single reflection or higher order reflections. Importantly, the neural network is trained on data distinct from the test environment, so no prior knowledge or calibration in the environment is required.

Finally, for the target navigation, we employ the following simple algorithm: When a link is classified as a LOS, strong single reflection, or strong single diffraction, the agent simply follows the direction of the strongest detected path. Otherwise, in absence of strong LOS or first-order reflection, the agent explores the environment using conventional SLAM methods, potentially using other sensor modalities such as camera or LiDAR.

The proposed method and analysis has a number of features that improve upon the state of the art:

- *Detailed antenna and multiple array modeling*: Practical mmWave devices at the terminal (UE) and base station (gNB) often use multiple arrays oriented in different directions to obtain 360 degree coverage [22], [23]. This work models these multiple array structures and also includes detailed models of the antenna element directivity in each array. In addition, we do not consider any local oscillator (LO) synchronization across different arrays.
- *Beam sweeping double directional estimation*: Many prior mmWave localization studies have either abstracted the directional estimation [19], considered single-sided directional estimates [17], [18], or considered double directional estimates using MIMO signaling [24], [25]. In this work, we modify the low-rank tensor decomposition algorithms in [20], [21] to account for both sweeping of the TX beams and use of multiple arrays at the TX and RX. Beam sweeping at the transmitter is critical to model for most cellular mmWave systems [26].
- *Novel neural network feature input*: Prior works such as [25] have used machine learning-based link state

classification using aggregate features of the paths such as the spread of the received power, delays or angles of the paths. In this work, we propose a neural network that takes the raw features of each detected path. This larger feature space is enabled by training the network on extensive data from ray tracing.

- *Multi-class link classification*: Instead of simply classifying the link as LOS or NLOS, we differentiate between four states: LOS, NLOS from a single interaction, higher-order NLOS and outage. We show that for target localization application, both LOS and first-order NLOS paths have angles of arrival that strongly correlate with good navigation directions.
- *Validation in realistic, complex environments*: The proposed approach is trained and tested on a large set of detailed indoor environments from the Gibson data set [27], that is widely-used in robotic navigation [28]. Each 3D model in the data set is imported to a state-of-the-art ray tracer [29], where we predict the wireless paths at 28 GHz. The wireless propagation data is then combined with realistic models of the arrays including the array sectorization and orientation and estimation algorithms.
- *Intra-site generalization ability*: We demonstrate that models trained on one set of environments generalize to completely new environments. Indeed, we show that, on new environments not in the training set, our link classification has a 88% accuracy.
- *Target localization demonstration*: The link state classification and angular estimation is combined with a state-of-the-art neural SLAM module [11] tested in AI Habitat robotic simulation environment [28] with the Gibson dataset above [27]. In addition to the detailed 3D models, the dataset includes LIDAR and camera data which are the typical inputs of the SLAM methods. We simulate the simple navigation policy that follows the estimated path when the detected link state is LOS or first-order NLOS; otherwise, the agent uses the exploration mode in the neural SLAM. We believe this is the first full end-to-end detailed simulation of mmWave wireless localization combined with state-of-the-art neural SLAM. In addition, we show that the proposed multi-class link state classifier significantly outperforms a policy that only uses the LOS classification.
- *Public dataset*: All the code and wireless data is made public, providing the first complete 5G wireless localization dataset combined with camera data and robotic simulation environment [30].

II. PATH ESTIMATION AND LINK STATE CLASSIFICATION PROBLEM

A. Overview

Before addressing the navigation problem specifically, in this section, we introduce a general problem of estimating multi-path components and the link state from mmWave measurements. To this end, consider a channel between a single TX and RX location. We assume a ray model where the channel is characterized by L discrete paths [31]. We will

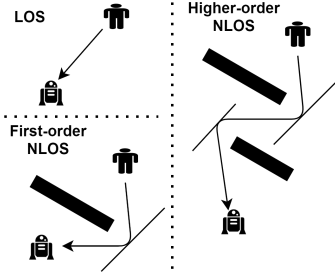


Fig. 2. A demonstration of the LOS, First-order NLOS, and Higher-order NLOS path.

only consider paths with gains above some threshold. As we will see below, the threshold is selected such that the path's parameters can be estimated accurately.

Now, each sufficiently strong path is either LOS or NLOS where any NLOS path arrives with one or more *interactions* such as diffractions, reflections, or transmissions. As shown in Fig. 2, we will classify the link as being in one of four states on the basis of the strongest received path:

- *LOS*: The strongest received path is above the minimum threshold and is LOS;
- *First-order NLOS*: At least one of received paths that are above the minimum threshold is NLOS with one interaction;
- *Higher-order NLOS*: All sufficiently strong paths from the TX to RX are NLOS with two or more interactions.
- *Outage*: There are no sufficiently strong paths above the minimum threshold.

Given this classification, we consider two problems:

- 1) *Path estimation*: Estimate the parameters (angles of arrival, angle of departure, relative delay and received SNR) for the strongest paths; and
- 2) *Link state classification*: Determine if the strongest path is LOS, First-order NLOS or Higher-order NLOS, or there is no sufficiently strong path.

As we will see below, the reason we are interested in this problem is that the angle of arrival of LOS and first-order NLOS path have strong correlation with the optimal direction for navigation. Hence, if can reliably detect the link state and estimate the angle of arrival of the strongest path, we can build a navigation system that simply follows the estimated strongest path angle of arrival.

B. Signaling and Array Modeling

We wish to realistically model the measurement of the signals from which the path estimation and link classification will be performed. To this end, we make the following assumptions:

Array Modeling: As discussed in the introduction, multiple arrays are critical in the mmWave range to provide 360 degree coverage [22], [23]. To this end, we assume that the TX and RX have, respectively, $N_{\text{arr}}^{\text{tx}}$ and $N_{\text{arr}}^{\text{rx}}$ mmWave arrays. We let $N_{\text{ant}}^{\text{tx}}$ and $N_{\text{ant}}^{\text{rx}}$ denote the number of antennas in each array. Since each array is typically designed to cover some angular region, we will sometimes refer to an array as a *sector*.

Although our simulations below consider only 2D localization, the methods are general and apply to 3D modeling as well. For 3D problems, we will use the notation $\Omega = (\phi, \theta)$ to denote an azimuth and elevation angle pair. In the case of 2D problem, $\Omega = \phi$ is the azimuth angle only with the elevation angle being ignored.

Now, for each potential RX angle, Ω^{rx} , we let $\mathbf{u}_{\text{rx}}(\Omega^{\text{rx}})$ denote the array signature across all the $N_{\text{arr}}^{\text{rx}}$ arrays. In general, a receive array signature represents the complex gains that would appear on a plane wave arriving from a given angle [31]. For the case of multiple arrays, we can write the received-side array signature as

$$\mathbf{u}_{\text{rx}}(\Omega^{\text{rx}}) = \left[\mathbf{u}_{\text{rx}}^{(1)}(\Omega^{\text{rx}}), \dots, \mathbf{u}_{\text{rx}}^{(N_{\text{arr}}^{\text{rx}})}(\Omega^{\text{rx}}) \right], \quad (1)$$

where $\mathbf{u}_{\text{rx}}^{(j)}(\Omega^{\text{rx}})$ is spatial signature from the j -th array at the RX. To model the arrays accurately, we will assume $\mathbf{u}_{\text{rx}}^{(j)}(\Omega^{\text{rx}})$ includes both the array gain and element gain. Also, to account for mutual coupling in densely-spaced arrays, we can apply the coupling matrix normalization as described in [32]. We will also assume the array spatial signatures are normalized such that $\|\mathbf{u}_{\text{rx}}^{(j)}(\Omega^{\text{rx}})\|^2$ is the directivity (in linear scale) of array j in the direction Ω^{rx} . At the TX side, we define $\mathbf{u}_{\text{tx}}(\Omega^{\text{tx}})$ similarly:

$$\mathbf{u}_{\text{tx}}(\Omega^{\text{tx}}) = \left[\mathbf{u}_{\text{tx}}^{(1)}(\Omega^{\text{tx}}), \dots, \mathbf{u}_{\text{tx}}^{(N_{\text{arr}}^{\text{tx}})}(\Omega^{\text{tx}}) \right]. \quad (2)$$

Finally, to consider the response on a single array, we introduce the following notation: Given a receive angle Ω^{rx} , let

$$\hat{\mathbf{u}}_{\text{rx}}(\Omega^{\text{rx}}) = \left[0, \dots, 0, \mathbf{u}_{\text{rx}}^{(j)}(\Omega^{\text{rx}}), 0, \dots, 0 \right], \quad (3)$$

with $j = \arg \max \|\mathbf{u}_{\text{rx}}^{(j)}(\Omega^{\text{rx}})\|^2$. Since $\|\mathbf{u}_{\text{rx}}^{(j)}(\Omega^{\text{rx}})\|^2$ is the directivity of the array j , $\hat{\mathbf{u}}_{\text{rx}}(\Omega^{\text{rx}})$ in (3) represents the array response on the array with the highest gain for the angle of arrival Ω^{rx} . Similarly, we define

$$\hat{\mathbf{u}}_{\text{tx}}(\Omega^{\text{tx}}) = \left[0, \dots, 0, \mathbf{u}_{\text{tx}}^{(j)}(\Omega^{\text{tx}}), 0, \dots, 0 \right], \quad (4)$$

where $j = \arg \max \|\mathbf{u}_{\text{tx}}^{(j)}(\Omega^{\text{tx}})\|^2$.

TX codebook: To enable detection, we assume the TX transmits a known synchronization signal, sweeping through a sequence of directions from the different TX arrays. Similar to (2), we can represent a TX beamforming vector with $N_{\text{arr}}^{\text{tx}}$ sub-vectors with $N_{\text{ant}}^{\text{tx}}$ components each representing the complex phases applied to the antenna elements. We will let $N_{\text{dir}}^{\text{tx}}$ denote the total number of TX directions. For each TX direction k , we will let \mathbf{w}_k^{tx} denote the TX beamforming vector for that direction. We will call \mathbf{w}_k^{tx} a *TX codeword*, the set of the TX codewords will be called the (multi-array) *codebook*.

Several methods can be used for 3D codebook design for mmWave systems (e.g. [23], [33]). In this work, we will simply assume the k -th TX codeword is of the form

$$\mathbf{w}_k^{\text{tx}} = \frac{1}{\|\hat{\mathbf{u}}_{\text{tx}}(\bar{\Omega}_k^{\text{tx}})\|} \hat{\mathbf{u}}_{\text{tx}}(\bar{\Omega}_k^{\text{tx}}), \quad (5)$$

where $\bar{\Omega}_k^{\text{tx}}$ is some angle of departure for the codeword and $\hat{\mathbf{u}}_{\text{tx}}(\bar{\Omega}_k^{\text{tx}})$ is as defined in (4). That is, \mathbf{w}_k^{tx} is aligned to the TX steering vector for some TX angle $\bar{\Omega}_k^{\text{tx}}$. We have used the

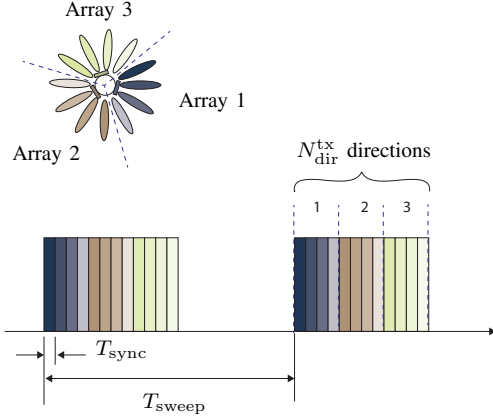


Fig. 3. Example TX beam sweeping with $N_{\text{arr}}^{\text{tx}} = 3$ arrays and 4 directions per array for a total of $N_{\text{dir}}^{\text{tx}} = 12$ beam directions. The synchronization signals are sent once in each direction with the pattern repeating every T_{sweep} seconds.

overline in the transmit angle $\overline{\Omega}_k^{\text{tx}}$ to differentiate the TX angle from the angles of the paths Ω_ℓ^{rx} that will be described below. The set of TX angles is the set

$$\left\{ \overline{\Omega}_k^{\text{tx}}, k = 1, \dots, N_{\text{dir}}^{\text{tx}} \right\}. \quad (6)$$

Observe that from (4), each TX codeword is transmitted on only one TX array at a time both to conserve power and not assume any local oscillator synchronization across TX arrays.

TX beam sweeping: In each of the $N_{\text{dir}}^{\text{tx}}$ directions, we assume the TX sends a known synchronization or reference signal of duration T_{sync} . Hence, the total time to transmit all $N_{\text{dir}}^{\text{tx}}$ directions is $T_{\text{sync}} N_{\text{dir}}^{\text{tx}}$. We assume the beam sweep pattern is repeated every T_{sweep} seconds with $T_{\text{sweep}} \geq N_{\text{dir}}^{\text{tx}} T_{\text{sync}}$.

An example is illustrated in Fig. 3 with $N_{\text{arr}}^{\text{tx}} = 3$ TX arrays and four directions per array for a total of $N_{\text{dir}}^{\text{tx}} = 12$ directions.

Wireless channel model: Let $x_k(t)$ denote the complex baseband synchronization signal sent in the k -th direction, $k = 1, \dots, N_{\text{dir}}^{\text{tx}}$. We assume a standard multi-path cluster model [31] where the corresponding received signal is given by

$$\mathbf{r}_k(t) = \sum_{\ell=1}^L g_\ell \mathbf{u}_{\text{rx}}(\Omega_\ell^{\text{rx}}) \mathbf{u}_{\text{tx}}(\Omega_\ell^{\text{tx}})^\top \mathbf{w}_k^{\text{tx}} x_k(t - \tau_\ell) + \mathbf{v}_k(t), \quad (7)$$

where \mathbf{w}_k^{tx} is the TX beamforming for direction k as given in (5), $\mathbf{r}_k(t)$ is the complex baseband signal across all $N_{\text{arr}}^{\text{rx}} N_{\text{ant}}^{\text{rx}}$ receive antenna elements, and $\mathbf{v}_k(t)$ is AWGN noise that we assume i.i.d. across RX antennas. In (7), L is the number of paths, and for each path ℓ , Ω_ℓ^{rx} and Ω_ℓ^{tx} are the RX and TX angles, $\mathbf{u}_{\text{rx}}(\Omega_\ell^{\text{rx}})$ and $\mathbf{u}_{\text{tx}}(\Omega_\ell^{\text{tx}})$ are the steering vectors of the arrays at those angles, g_ℓ is the complex path gain, and τ_ℓ is the path delay. For simulation, one can generate the path parameters via statistical models such as [34], although as we will discuss below, in this work the path parameters will be found from ray tracing.

III. PROPOSED ALGORITHM FOR PATH ESTIMATION AND LINK STATE CLASSIFICATION

A. Path Estimation via Low-Rank Tensor Decomposition

For the path estimation, we adapt a commonly-used low rank tensor decomposition method [20], [21] with modifications to handle the multiple arrays and TX beam sweeping. Define the spatial and temporal correlation

$$\rho_k(\tau, \Omega^{\text{rx}}) := \int \hat{\mathbf{u}}_{\text{rx}}(\Omega^{\text{rx}})^* \mathbf{r}_k(t) x_k^*(t - \tau) dt, \quad (8)$$

which is a complex function of the TX angle k , RX angle Ω^{rx} and delay τ . Under the channel model (7), the signal will contribute one peak in the correlation magnitude $|\rho_k(\tau, \Omega^{\text{rx}})|^2$ for each path ℓ when $(\tau, \Omega^{\text{rx}}) = (\tau_\ell, \Omega_\ell^{\text{rx}})$ when the TX direction Ω_ℓ^{tx} is closely aligned the transmit angle $\overline{\Omega}_k^{\text{tx}}$. Thus, in principle, we can locate the paths from the peaks in the correlation function.

Following [20], [21], we use a low-rank tensor decomposition to extract these peaks. Specifically, we first select a discrete set of delays and RX angles:

$$\tau = \bar{\tau}_i, \quad i = 1, \dots, N_{\text{dly}}, \quad (9)$$

$$\Omega^{\text{rx}} = \overline{\Omega}_j^{\text{rx}}, \quad j = 1, \dots, N_{\text{dir}}^{\text{rx}}, \quad (10)$$

where N_{dly} is the number of delay hypotheses and $N_{\text{dir}}^{\text{rx}}$ is the number of RX angular directions. Again, note that we use the overlines in $\bar{\tau}_i$ and $\overline{\Omega}_j^{\text{rx}}$ to differentiate them from the true delays and angles τ_ℓ and Ω_ℓ^{rx} . We then evaluate the complex correlation (8) at the discrete values to obtain a third-order tensor:

$$S[i, j, k] = \rho_k(\bar{\tau}_i, \overline{\Omega}_j^{\text{rx}}). \quad (11)$$

As described in [20], [21], we then find an approximate low-rank decomposition,

$$S[i, j, k] \approx \sum_{\ell=1}^R a_{\ell i} b_{\ell j} c_{\ell k}, \quad (12)$$

where R is the estimated rank, and \mathbf{a}_ℓ , \mathbf{b}_ℓ and \mathbf{c}_ℓ are the basis vectors for each rank one term in the delay, RX angle and TX angle dimensions. Any low-rank tensor decomposition method can be used (see, e.g. [35] for a survey). In this work, we will use two-way PCA by first performing PCA flattening the (j, k) dimensions and then performing PCA on the (j, k) matrix.

Following the low-rank tensor decomposition, we can estimate for the delays, TX and RX angles can be found from the peaks in the basis vectors:

$$\hat{\tau}'_\ell = \bar{\tau}_i, \quad i = \arg \max |a_{\ell i}| \quad (13a)$$

$$\hat{\Omega}'_\ell^{\text{rx}} = \overline{\Omega}_j^{\text{rx}}, \quad j = \arg \max |b_{\ell j}| \quad (13b)$$

$$\hat{\Omega}'_\ell^{\text{tx}} = \overline{\Omega}_k^{\text{tx}}, \quad k = \arg \max |c_{\ell k}|. \quad (13c)$$

Since we do not assume timing synchronization between the TX and RX, the estimated delays $\hat{\tau}'_\ell$ are only meaningful as *relative* values. For this reason, we convert the raw delay estimates to relative delay estimates

$$\hat{\tau}_\ell = \hat{\tau}'_\ell - \min_{\ell=1, \dots, K} \hat{\tau}'_\ell. \quad (14)$$

We can also estimate the RX SNR of the path as:

$$\gamma_\ell := \frac{\|\mathbf{a}_\ell\|^2 \|\mathbf{b}_\ell\|^2 \|\mathbf{c}_\ell\|^2}{E_{\text{avg}}}, \quad (15)$$

where the numerator represents the total energy along the estimated ℓ -th direction and the denominator is the average energy per sample,

$$E_{\text{avg}} := \frac{1}{N_{\text{dly}} N_{\text{dir}}^{\text{tx}} N_{\text{dir}}^{\text{rx}}} \sum_{ijk} |S[i, j, k]|^2.$$

The resulting procedure thus produces a set of path estimates

$$\left\{ (\hat{\tau}_\ell, \hat{\Omega}_\ell^{\text{rx}}, \hat{\Omega}_\ell^{\text{tx}}, \gamma_\ell), \ell = 1, \dots, K \right\}, \quad (16)$$

that includes the relative delay, RX and TX angles and SNRs of the path. We will fix K in this work since we have an SNR indication γ_k to discard low energy paths.

B. Configuration and Synchronization Issues

The methods described above apply to any scenario where the target device can transmit a mmWave beam sweeping synchronization signals. Such signals are commonly used in mmWave RADAR and can be used in this application if the target can carry a RADAR transmitter. If the target device has a standard 5G mmWave device, then the existing management and positioning signals may be used [7], [8], [36], but some additional configuration capabilities may be needed. For example, if the target is a 5G UE device, the path estimation could potentially be performed from the uplink sounding reference signals (SRS). The mobile agent could then attempt to listen to the SRS signals for localizing the target. Of course, normally the SRS are directed to the serving base station. Hence, for the signaling method described above, the UE would need to receive some configuration from the network to transmit the SRS in a sweeping pattern. Also, if the UE does not have a connection to a mmWave base station (a likely scenario since the target may be inside where the mmWave signals are blocked), the UE would need to be configured over a sub-6 GHz carrier and be permitted to transmit even in absence of a detected network.

Whichever signals are used, one issue is the transmit synchronization. For the mobile agent RX to know the transmit angle, $\hat{\Omega}_\ell^{\text{tx}}$ in (16), the RX would need to know which beams are being transmitted at which times. In addition, the TX would need to inform the RX of the TX directions. In the cellular case, this information would also need to be conveyed in the configuration. Since this may not always be possible, we investigate in the simulations below the cases when the TX angles is and is not available.

C. Link State Classification Neural Network

The next step is to classify the link state (LOS, First-Order NLOS, Higher-Order NLOS or Outage) from the parameter estimates (16) of the detected paths. We use the estimates from a fixed number, $K = 5$, paths, taking the paths with the *strongest* estimates SNRs. In general, increasing the number of paths increases the number of features in our model and

hence can result in over-fitting. We found $K = 5$ to provide the lowest generalization error. Note that we take the $K = 5$ *strongest* paths, not the K *earliest* paths. Hence, we do not miss any strong paths that arrive late.

Since the data (16) are heterogeneous, we then transform the inputs to a common scale – a critical step to use neural networks. Although the methods can be applied for 3D angles, for the remainder of the paper, we will focus on 2D problems that only use the azimuth angles. That is, the angle estimate $\hat{\Omega}_\ell^{\text{tx}}$ $\hat{\Omega}_\ell^{\text{rx}}$ are scalar azimuth angles. These angles are in the range $[-\pi, \pi]$, and are scaled from $[-1, 1]$. The SNR parameter γ_ℓ are transformed to scaled value in $z_\ell \in [0, 1]$ with the transformation

$$z_\ell = \max \left\{ 0, \min \left\{ 1, \frac{\gamma_\ell - \gamma_{\min}}{\gamma_{\max} - \gamma_{\min}} \right\} \right\}, \quad (17)$$

for some fixed parameters γ_{\min} and γ_{\max} . Under the scaling (17), paths weaker than the threshold γ_{\min} result in $z_\ell = 0$ and very strong paths ($\gamma_\ell \geq \gamma_{\max}$) are mapped to $z_\ell = 1$. We used fixed limits $\gamma_{\min} = 5$ dB and $\gamma_{\max} = 50$ dB. Also, when less than K paths are detected, we set the corresponding scaled SNR values to zero to indicate the path does not exist.

For the delays, we measure the values relative to the first detected path (14). Subtracting the first path is required since we do not assume absolute timing. We then scale the relative delays by a fixed value of 100 ns which corresponds to 30 m of propagation distance.

In total, the pre-processing results in scaled values of the four parameters of the each paths (16). With data from $K = 5$ paths, the neural network takes as an input $4K = 20$ values. If the TX angles $\hat{\Omega}_\ell^{\text{tx}}$ are not assumed to be available, then the neural network will have 3 values per path with a total of $5(3) = 15$ values. As we will describe below, we will then apply a simple 2 layers fully connected network. The output is a four-way softmax for the four link states, LOS, First order NLOS, High order NLOS and Outage.

IV. CREATION OF THE ROBOTIC AND WIRELESS DATASET

We validate the methods on the AI Habitat robotic simulation environment [28] with the Gibson 3D indoor models [27]. Gibson's underlying database of spaces includes 572 full buildings composed of 1447 floors covering a total area of 211 000 m². The indoor environments include complete 3D camera and LiDAR data, and maps from actual interior environments. These 3D models can be imported into the AI Habitat simulation that includes a complete kinematic model of the robots. The simulation environment has been widely-used for validating indoor SLAM and navigation algorithms, see e.g. [37], [38].

One key contribution of this work is to augment this dataset with a wireless coverage maps. This will create what we believe is the first dataset with camera, LiDAR and wireless data integrated into a robotic simulation environment. In addition to validating the algorithms in this work, the dataset can be used for other positioning work as well as cloud robotics experiments with wireless connectivity.

To capture the wireless coverage, we use the powerful ray tracing package, Wireless InSite by Remcom [29] which has

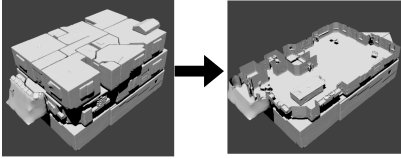


Fig. 4. Most 3D models in the Gibson data set are of multi-storey residences. In this example, the left figure shows a three storey house. We extract the second floor, as shown on the right, to generate our test layout.



Fig. 5. A typical indoor environment in the Gibson data set [27] with furniture, plants, and irregular building structures that significantly increases computational load for ray tracing.

also been used in several other recent mmWave studies such as [39]–[41]. Ray tracing uses a high-frequency approximation to simulate the electromagnetic paths between any two locations. As the Gibson dataset contains highly detailed and fine-grained 3D models, we need to pre-process them in order to reduce the computational effort when we use them as ray tracing environments. Since we consider the navigation and positioning problems in 2D and most of the buildings in the data set are multi-story residence buildings, we first select and extract one floor from each – an example is shown in Fig. 4.

Next, as shown in Fig. 5, the indoor environment contains furniture, plants, and irregularly constructed structures. These objects often have many non-smooth reflecting surfaces, which significantly increases the amount of computing required for the ray tracing. To simplify the 3D model, we utilize Habitat-Sim [42], [43] to capture a floor plan – making the model essentially 2D. Also, as far as possible, the irregular and uneven walls, ceilings, and floors of the original 3D model are transformed into smooth planes. The edges of the simplified 2D floor plan are then vertically extended to create walls. The resulting 3D map can then be imported to Remcom Wireless InSite – See Fig. 6.

For each imported map, we then place the transmitters in 10 randomly selected locations representing 10 possible target positions. The ray tracing is then used to estimate the wireless paths at RX locations on a 160×160 grid with 0.15×0.15 m grid representing a total area of 24 m^2 . Example ray tracing simulation areas are shown in Fig. 7.

The ray tracing is performed at 28 GHz, the most commonly-used frequency for 5G mmWave devices [44]. We ignore the difference of material and treat all walls as the ITU (International Telecommunication Union) layered drywall whose permittivity is 2.94 (F/m) and conductivity is 0.1226 (S/m) in 28 GHz.

For each TX-RX location, the ray tracing produces an estimate of the set of large scale parameters

$$(g_\ell, \Omega_\ell^{\text{rx}}, \Omega_\ell^{\text{tx}}, \tau_\ell), \quad \ell = 1, \dots, L,$$

for the paths in the channel model (7). Example ray tracing

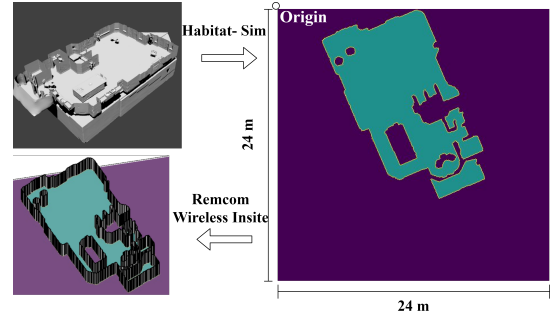


Fig. 6. An example of a 24×24 meter indoor environment map generated by the Habitat-Sim [42]. The Wireless InSite tool by Remcom [29] uses the top-down map to rebuild a 3D indoor model. Some assumptions are made to reduce the high computational costs of ray tracing.

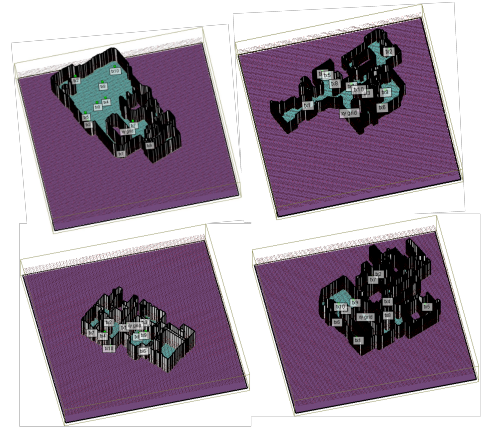


Fig. 7. Four examples of ray tracing simulation area. In each map, green dots represent transmitter locations and the red dots represent the receiver grid with total 25,600 receivers.

outputs are shown in Fig. 8. Using the true signal parameters, we can then simulate the path estimation algorithms in Section III to create estimates of the path parameters (16). The specific parameters for the arrays and transmitter are discussed in the next section.

In total, the procedure is run on 38 unique environments from the Gibson dataset with 10 TX locations in each environment. For each environment and TX location, the ray tracing results in a map of the true wireless paths at each RX location. The path estimation simulation creates a second map of the estimated paths at each RX locations. Combined with the original Gibson data, we have thus created a unified dataset where 3D models with camera and LiDAR data are augmented with wireless ray tracing and wireless path estimation. The dataset is made available in [30].

V. PATH ESTIMATION AND LINK STATE CLASSIFICATION SIMULATION RESULTS

In this section, we describe the simulation parameters and measured performance of the path estimation and link state classifier on the data set in Section IV. We will discuss the integration with navigation in the subsequent section.

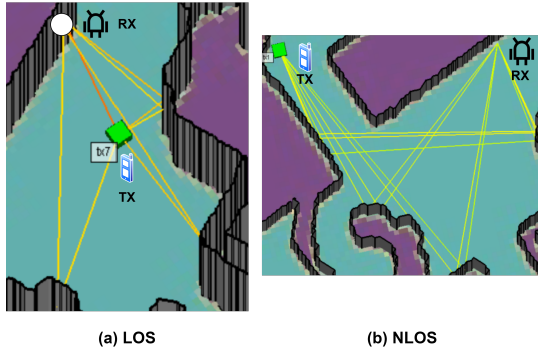


Fig. 8. LOS (left) and NLOS (right) examples of the ray tracing paths. (Some weaker paths are not shown).

TABLE I
PATH ESTIMATION SIMULATION PARAMETERS

Item	Value	
	UE	gNB
Carrier	28 GHz	
Bandwidth	400 MHz	
Antenna element	Microstrip patch antenna	
Number of Arrays	3 [46]	
Array Size	8 (1×8 ULA)	16 (4×4 UPA)
Transmit Power	23 dBm	
Losses	6 dB including noise figures [47]	
Number beams	24	48

A. Array Modeling

We assumed a 28 GHz array similar to several recent published 5G designs and layouts [22], [45]. The parameters for the arrays and signaling are shown in Table. I. The target TX is assumed to be a UE device and the RX is a gNB. The arrays use microstrip patch antennas and the beam patterns of each array when directed at boresight are shown in Fig. 9.

As in [22], we create the multiple antenna arrays at both the gNB and UE. Specifically, we assume three arrays with azimuth angles 0° , 120° , and -120° and 0° elevation. The multi-sector layout provides 360° coverage. For example, Fig. 10 plots the maximum gain for each individual array and the maximum gain over all three arrays over $[-180^\circ, 180^\circ]$ the azimuth directions. We see that the minimum gain is only approximately 3 dB below the maximum.

For the beam search codebook at the gNB, we simply use the beams on 48 angles uniformly spaced in $[-180^\circ, 180^\circ]$ in the azimuth direction. Since the gNB has 16 elements per array and three arrays, the use of 48 beams corresponds to the number of orthogonal spatial degrees of freedom. Similarly, in the UE we use 24 beams.

B. Path Estimation

As shown in Table I, the TX power was set to 23 dBm with a sample rate of 400 MHz – standard in 5G deployments [44]. For the positioning signal, we transmitted a 2048 sample random waveform for a total of duration of $5.1 \mu\text{s}$ to enable the signal to be transmitted entirely in one 5G NR OFDM symbol. The correlation (8) was performed via an FFT. Since the positioning accuracy is only dependent on the sample rate,

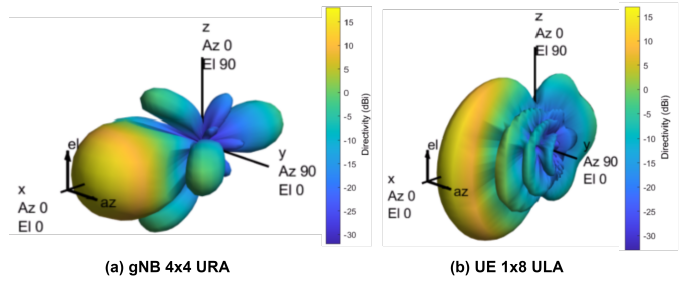


Fig. 9. The pattern of a gNB antenna array and a UE antenna array. Arrays are aligned so that its bore-sight is on the x-axis. An antenna's directivity is a component of its gain. When the target is located in the main lobe (yellow areas in the figure), the maximum antenna gain is received.

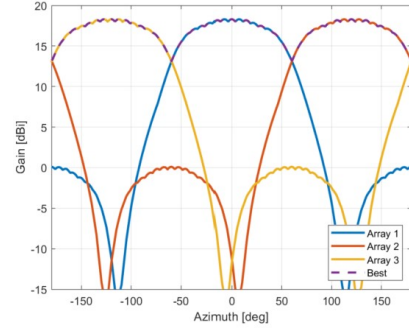


Fig. 10. Array gain including the element gain from each gNB array as well as the best for all three arrays. We see that by using multiple arrays we can obtain full azimuth coverage.

duration and power — such as those used in 3GPP positioning [4]–[8] — would have resulted in similar performance.

The tensor decomposition path estimation algorithms in Section III were then run at each location. Fig. 11 depicts a result of the estimated paths at one LOS location (left) and NLOS location (right). The red circles represent the angular locations of true paths where you can clearly observe path clusters from the scattered reflections and diffractions. The black squares are the estimated path locations and generally extract the cluster centers.

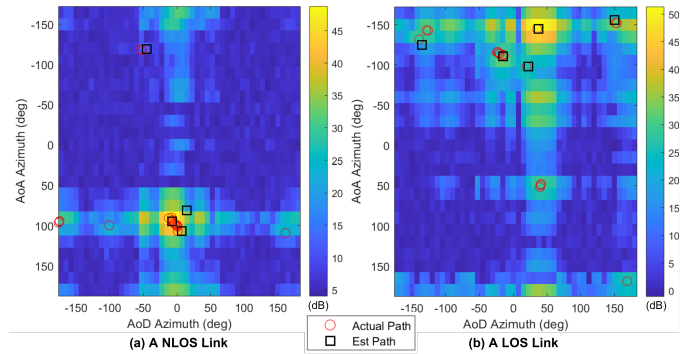


Fig. 11. Example received power spectrum along TX-RX direction pair along with the location of the actual ray tracing paths of a LOS link and a NLOS link. The black squares indicate the result of path estimation by the low-rank tensor decomposition in Section III.

The overall accuracy of the method is depicted in Fig. 12 which shows the CDF of the AoA error on the strongest

path across the 38 environments and 10 transmitter locations described in the dataset in Section IV. The CDF is plotted separately for LOS and NLOS cases with the NLOS case plotted separately for the case of first-order and higher-order NLOS. We see that the strongest path's AoA errors differ greatly between the three link states. Indeed, 98% of LOS links and 85% of first-order NLOS links have errors less than 5° . In contrast, for higher-order NLOS links, more than 40% of errors are larger than 10° . For this reason, the angular estimates for the LOS and first-order NLOS links are much more reliable when used for navigation.

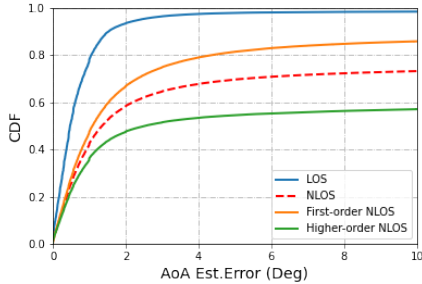


Fig. 12. Distribution of the absolute error between the estimated strongest path's AoA from channel sounding and the AoA of the strongest path in real ray tracing data set.

C. Link State Classification

We next evaluated the link state neural network described in Section III-C. Our network attempts to classify the link state (LOS, First-Order NLOS, Higher-Order NLOS, and outage) from the estimated path parameters (16). As inputs, we use the parameters from the $K = 5$ *strongest* detected paths. The parameters of this link-state neural network are shown in Table II. When the TX angle is available, there are 4 parameters per path for a total of $4K = 20$ inputs. We use a simple fully connected neural network with two layers with 8 and 6 hidden units with the ReLU activation [48]. We also compare our neural network method to a modified method from [25], one of the best prior work algorithms. In paper [25], Huang and Molisch et al. propose the machine learning based LOS and NLOS identification methods for the MIMO system in vehicle-to-vehicle (V2V) networks. The method of [25] uses a set of custom features (static and time-varying characteristics), while our proposed approach uses the raw MPC (the multipath component) data.

The network is trained on 18 of the 38 environments and tested on the remaining 20. As described in Section IV, each environment has 10 TX locations. We train and test only on the valid indoor RX locations in each map. The resulting total training set contains 483690 unique TX-RX links while the validation set contains 563810 unique TX-RX links.

We train this network with links from a set of training maps, resulting in a pre-trained link-state classification neural network. We tested the robot's navigation algorithms on a other set of different maps. It should be emphasized that the test maps are completely new environments relative to

TABLE II
LINK STATE NEURAL NETWORK CLASSIFIER CONFIGURATION

Parameter	Value
Number of inputs	20
Hidden units	[8, 6]
Number of outputs	4
Optimizer	Adam
Learning rate	0.001
Epochs	300
Batch size	1024

the robot, which also shows that our pre-trained link-state classification neural network can be extended to any unknown new indoor environment.

We use the Adam optimizer [49] with a learning rate of 0.001 for 300 epochs. The loss is shown in Fig. 13, and the accuracy is shown in Fig. 14. The yellow line represents the accuracy of validation, while the blue line represents the accuracy of training. From Fig. 14, we see that our model's validation accuracy reached 88% after approximately 100 epochs, while the modification of prior method obtains 84%. The main contribution of our network is considering first-order NLOS versus higher-order NLOS (a four-way link-state classifier), not this increase in accuracy.

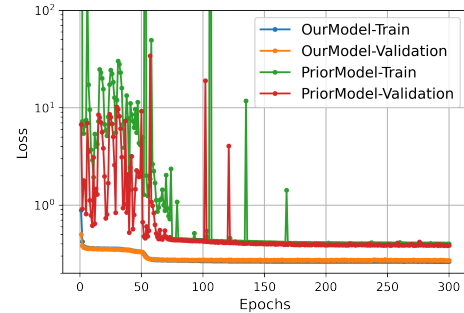


Fig. 13. Loss of the link-state classification neural networks.

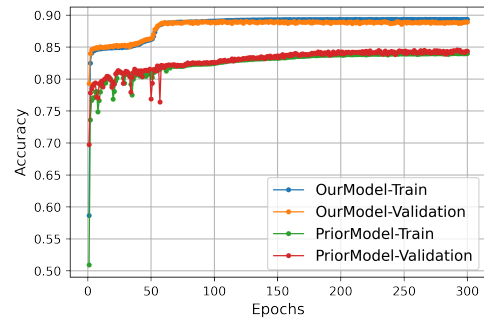


Fig. 14. The 18 maps are used as the training set and the other 20 maps are used as the test set. The yellow line shows the validation accuracy of our model which reached about 88% after about 100 epochs.

To visualize the errors, Fig. 15 plots the true and predicted link states in a typical environment. The true link state (as predicted by ray tracing and shown on the left) consistent with

common sense. In particular, all RX locations where the TX can be directly seen are in the LOS state. From the right figure, we see that the link state is predicted mostly correctly, but there are some errors. For the most part, the estimates are conservative meaning an LOS state is predicted as first-order NLOS, or first-order NLOS predicted as higher-order NLOS.

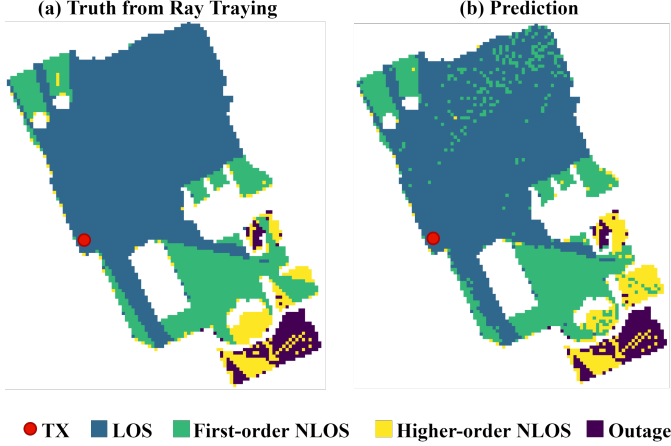


Fig. 15. Two Link-States maps. (a) is truth from ray tracing tool and (b) is result of the link-states classification neural network prediction.

Finally, it is interesting that one can distinguish first-order and higher-order LOS so accurately. Of course, from a *single* multi-path component, one cannot know if it arrived via one or more reflections. However, the neural network demonstrates that the *joint* statistics across multiple path components can reveal the number of reflections with a high accuracy in completely new environments not part of the training data set.

D. Removing the TX Angle Information

As described in Section III-B, the TX angle estimate ($\hat{\Omega}_\ell^{\text{tx}}$ in (16)) may not always be available as it requires synchronization and knowledge of the TX codebook at the RX. To study the effect of removing the TX angle, we re-trained and re-evaluated the link classifier performance when the TX angle is removed.

Fig.16 plots the confusion matrix of the validation data set using only RX angle (AoA) and RX and TX angle (AoA+AoD). With the exception of a very small difference in the outage state, the accuracy of using AoA degrades performance somewhat. For example, without using the AoD estimate, the accuracy of LOS state decreases from 96% to 88%. Furthermore, the AoA-only method incorrectly classifies 25% of the LOS links and the first-order NLOS state. For the remainder of the paper, we will assume we have the TX information, although localization without TX information is an area of future work.

VI. INTEGRATION WITH ACTIVE NEURAL-SLAM

A. Overview of Active Neural-SLAM

We conclude by integrating the path estimation and link state classification into the state-of-the-art Active Neural-SLAM algorithm of [11] to perform the target localization. We

Outage	1	0	0	0	1	0	0	0
LOS	0	0.88	0.11	0.0052	0	0.96	0.034	0.0046
First NLOS	0	0.14	0.74	0.12	0	0.058	0.8	0.14
Higher NLOS	4.9e-05	0.0059	0.19	0.81	0.00011	0.0037	0.17	0.83
	Outage	LOS	First NLOS	Higher NLOS	Outage	LOS	First NLOS	Higher NLOS
	(a) AoA				(b) AoA+AoD			

Fig. 16. The confusion matrix of the validation data set on only AoA method and AoA+AoD method. AoA+AoD method improves the classification performance in LOS, first-order NLOS, and higher-order NLOS links.

first review the basics of the Active Neural-SLAM algorithm of [11].

Neural-SLAM is a powerful new method for agent navigation in unseen environments, sometimes referred to as *exploration*. Exploration is a critical task in building intelligent agents. In exploration, the goal of the agent is to explore as much area as it can and as fast as possible. Efficient exploration in a large environment requires the agent to effectively map and memorize the already seen environment, estimating its current state/pose and plan the next actions. Traditional machine learning methods to learn to explore have been successful, but these methods generally require end-to-end reinforcement learning (RL) making the task of exploration difficult in large environments and increase the sample complexity. Instead, Devendra *et. al.* [11] recently proposed Active Neural-SLAM (see the lower half of Fig. 17) which uses structured spatial representations, hierarchical policies and search based planners. The Active Neural-SLAM consists of three components: Neural-SLAM (f_{SLAM}), Global Policy (π_G), and Local Policy (π_L). The Neural-SLAM component is trained using a supervised learning approach to predict the top-down 2D map and estimate the agent's current pose based on the incoming RGB camera images and sensor pose readings. The Global policy is trained using RL with rewards proportional to the increase in coverage. The Global policy takes as input the predicted top-down 2D map and the estimated agent's pose from the Neural-SLAM component to output a long term goal on the map. Given the long-term goal, predicted top-down map and agent pose estimate, a Fast Marching planner computes the shortest path from the current agent location to the long-term goal in the unexplored area on the map. A short-term goal is generated on this planned path at a farthest point within 0.25 m of the agent's current location. The local policy is trained using imitation learning, wherein it takes input as RGB camera images and short term goal to output a navigational action. Active Neural-SLAM uses AI Habitat Simulator and is shown to out-perform existing end-to-end RL methods and other baselines on Gibson and Matterport datasets for exploration tasks.

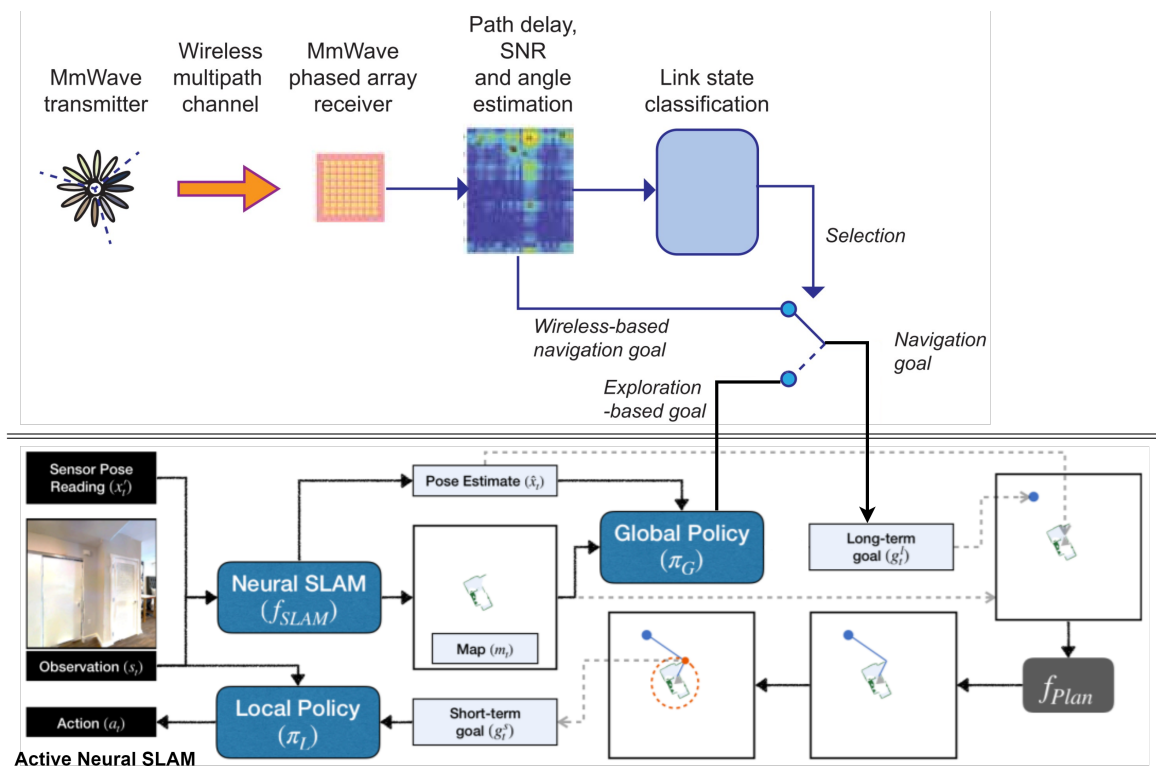


Fig. 17. MmWave-Based wireless path detection and link state classification are used to augment the Active Neural-SLAM module [11] by overwriting the navigation goal from the wireless path estimation.

B. Integration of Wireless Information for Target Discovery

The modular structure of the Active Neural-SLAM framework provides a simple method to add wireless information for the target discovery problem. As mentioned in the Introduction, suppose the mobile agent must locate and navigate to target. The target's location is not known, but it broadcasts positioning signals. To navigate to the target we can augment the Active Neural-SLAM module with the wireless signal processing, shown in the top half of Fig. 17.

As described above, the mobile agent will have a wireless receiver and can estimate the wireless paths and their angles of arrivals (AoAs). If the target was known to be in a LOS state, and the AoA was reliable, the agent could simply follow the AoA of the strongest path. In Fig. 17, this navigation goal is referred to as the "wireless-based navigation goal".

Of course, the link state and the path estimate are not known *a priori* by the mobile agent. We thus propose to use the link state classification along with the estimated SNR of the strongest path to make a decision on whether to use the wireless-based navigation goal or not. If the wireless-based navigation goal is selected, it can simply overwrite the navigation goal in the Active Neural-SLAM module. If, on the other hand, the wireless-based navigation goal is considered unreliable, the mobile agent can use the exploration-based goal from the original global policy. This selection concept is illustrated in Fig. 17.

The resulting algorithm structure thus attempts to use the wireless based AoA when it is accurate, but goes back to the exploration when the wireless signals are not reliable or not

likely to point into a useful direction to the target.

We consider three possible selection algorithms for determining whether or not to use the estimated AoA from the wireless detection:

- *AoA based on SNR only*: The robot follows the AoA of the highest SNR path if the path SNR is above some threshold in any link state. Otherwise, the robot follows the goal from Active Neural-SLAM map exploration.
- *AoA when LOS*: The robot follows the estimated AoA when the strongest path is in a LOS state and the SNR is above the threshold.
- *AoA when LOS or First-order NLOS*: The robot follows the estimated AoA when the strongest path is in a LOS state or first-order NLOS and the SNR is above the threshold.

In the simulations below we use a minimum SNR threshold of 10 dB for all three options, which we found to give the best results. Note that the second and third options require link state classification and the third option requires differentiation between first-order and higher-order NLOS.

To better evaluate the performance of our proposed *AoA when LOS or First-order NLOS* wireless assisted algorithm, we use a state-of-the-art completely computer vision-based navigation algorithm which calls the *Visual LOS CV-Based SLAM* navigation algorithm. The *Visual LOS CV-Based SLAM* navigation algorithm is defined as that: the robot first starts to use the Active Neural-SLAM algorithm [11] to explore the unknown environment, and as soon as the target appears in the robot's field of view, we assume that the robot uses a

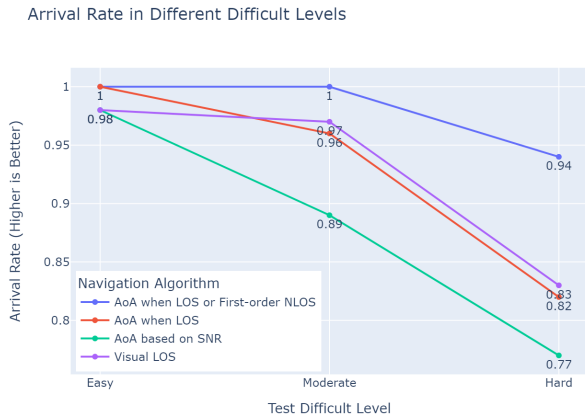


Fig. 18. The arrival success rate of three algorithms in easy, moderate, and hard environments. Our proposed *AoA when LOS or First-order NLOS* wireless assisted algorithm has the highest arrival success rate in all test levels, and it beats the stat-of-art completely computer vision-based navigation algorithm.

computer vision technology to identify and locate the target with 100% accuracy, and then finally the robot sets the goal on the position of the target and navigates itself.

C. Evaluation

To evaluate different algorithms, we compared them to a *baseline* algorithm where the robot knows the position (coordinates) of the target (TX) and always sets walking-goal at the TX. The baseline is essentially an oracle that provides an upper bound on the performance of any algorithm that does not know the TX location.

The baseline algorithm also provides a simple classification of the environments. Twenty validation maps with a total of 193 independently validated tests were run. Based on the number of steps taken by the robot to reach the destination of the baseline algorithm, we classified the tests into three difficulty levels: easy, moderate, and hard. And there are 52 easy tests, 76 moderate tests, and 65 hard tests. We will present the results separately for these cases.

In order to evaluate the performance of an algorithm, we rely on two criteria: arrival success rate and arrival time. The robot is defined to have succeeded at arriving at the destination if it arrives at the TX location within 1000 steps. The arrival success rate (sometimes, simply arrival rate) is the fraction of the number of time of the robot succeeds in arriving. In the case of a successful arrival, the arrival time is measured relative to the baseline algorithm. As a result, an algorithm with the lowest arrival time and highest arrival success rate is preferable.

Fig. 18 plots the arrival success rates for the four algorithms in the easy, moderate and hard environments. We see that without the assistance of the link-state classification neural network, the robot using the *AoA based on SNR only* algorithm gets stuck and is unable to succeed in 11 percent of the moderate tests and 23 percent of the difficult tests. At the same time, the *AoA when LOS or First-order NLOS* algorithm

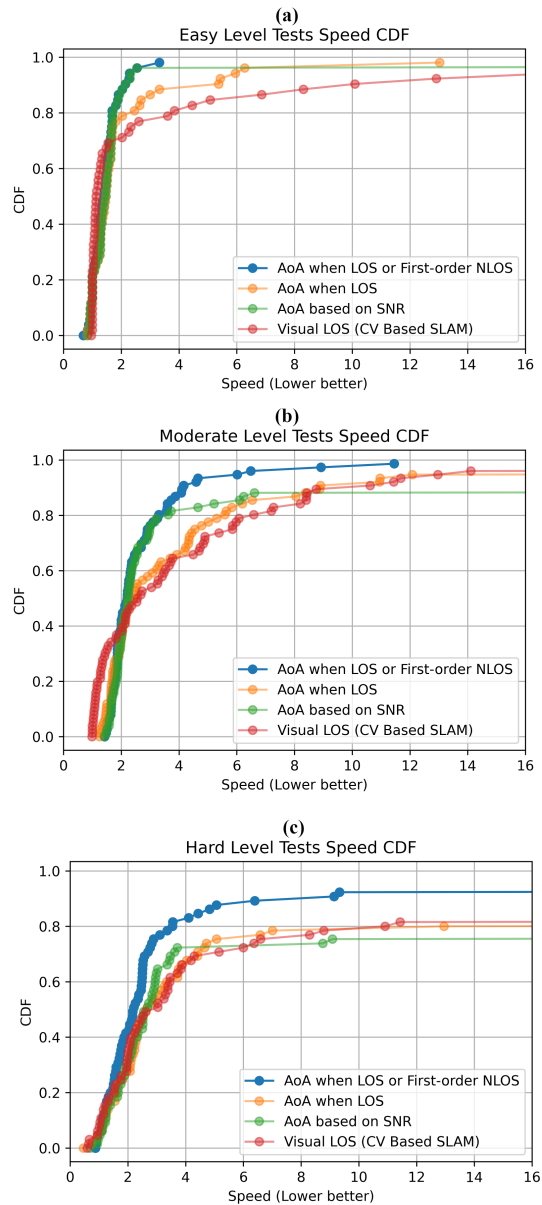


Fig. 19. Three cumulative distribution function (CDF) plots show the arrival speed in easy, moderate, and hard difficult level. At the moderate and hard difficulty levels, our proposed *AoA when LOS or First-order NLOS* wireless assisted algorithm performs most effectively. The results demonstrate the effectiveness of the four-way link-state classification neural network in improving the robot indoor navigation problem.

is superior to *AoA when LOS*. This result suggests that the four-way link state classification provides a more robust metric for using the wireless information. The reason for this is that even though the estimation error of AoA in the first-order NLOS is larger than the LOS, the robot can still use the AoA information to navigate itself and avoid getting stuck with high probability. As we use the beam sweeping double directional path estimation for both AoA and AoD, our link-states classification neural network shows high accuracy in identifying LOS, first-order NLOS, and higher-order NLOS. Since the estimation error of AoA varies greatly under the three different link states, as shown in Fig. 12, we consider

that using the angular information in the wireless signal to help navigation in the case of LOS and first-order NLOS is the optimal solution which can reach a highest arrival rate. In addition, the *AoA when LOS or First-order NLOS* wireless assisted algorithm is the only one that defeats the state-of-the-art completely computer vision-based navigation algorithm in all three difficult levels. As a result, the robot can utilize the information provided by the wireless signal to the maximum extent without being affected by the noise in the wireless communications that may cause the robot to move in the wrong direction.

In order to analyze the arrival time, Fig. 19 plots the cumulative distribution functions (CDFs) of the arrival time for the different algorithms in the three difficulty levels. Instances where the algorithm did not succeed as arriving are treated as a big arrival time. Note that the arrival times are relative to the baseline with an arrival time of one being optimal.

We see that in all three difficult levels, the arrival time of *AoA based on SNR only* and *AoA when LOS only* algorithms are slightly better than the *Visual LOS CV-Based SLAM* navigation algorithm, which means that without a link-state classification or with a three-way (LOS, NLOS, outage) link-state classifier, the mmWave wireless system have very limited optimization of the state-of-the-art completely computer vision-based navigation algorithm. However, with our new four-way link-state classifier (LOS, first-order NLOS, higher-order NLOS, outage), the *AoA when LOS or First-order NLOS* wireless assisted algorithm performs most effectively in moderate and hard level tests.

D. Representative Example

It is useful to look at a representative example, to visualize the problems with navigation without the link state classification. Fig. 20 shows the predicted map and route followed by robot with *AoA when LOS or First-order NLOS* on the top panel and *AoA based on SNR* on the bottom panel. The robot is started at the same location in both cases. In this case, the starting point are in higher-order NLOS link-state. In the *AoA based on SNR* algorithm, the robot follows the AoA. Since it is a high-order LOS, the direction is not valuable even if it is reliably detected. As a result, the robot spends a significant amount of time in the area framed by the black dashed line in Fig. 20(b). In contrast, the *AoA when LOS or First-order NLOS* algorithm successfully detects that the location is a high-order NLOS state. The robot then ignores the AoA initially and instead relies on the Active Neural-SLAM exploration which rapidly takes it into a new area.

VII. CONCLUSIONS

We have considered using mmWave-based positioning for target localization in unknown environment. This problem is relatively new in the context of mmWave-based localization. We have considered an algorithm that uses advanced wireless path estimation and link state classification methods and integrated these into a state-of-the-art neural SLAM module for complete robotic navigation. Our results demonstrate that



Fig. 20. An example of two different robot walking paths are generated in a test case. In (a), the robot uses the *AoA when LOS or First-order NLOS* and spends 150 steps to arrive the TX. In (b), the robot uses the *AoA based on SNR* and spends 358 steps to reach the TX. The area framed by the black dashed line shows the difference between the two algorithms.

target navigation is possible, even in challenging new environments. In particular, the results demonstrate the importance of accurately determining the link state including differentiating between first-order and higher-order NLOS states.

The proposed method is, however, a starting point and there are several open avenues for future work. Most obviously, the wireless and visual sensor data are not currently processed jointly: the proposed algorithm uses one or the other at any given time. Moreover, in the proposed approach, the wireless information is not used for SLAM, only for localization. There is now a large body of work on mmWave SLAM [3], [50] and one avenue of future work is to incorporate these or other methods. Indeed, the camera and RF signals represent a “digital twin” from one another with significant possibilities for joint processing. More broadly, there is a rich interplay between visual processing, wireless sensing and navigation. To assist future work in this area, we have developed a fully open source data set [30] that integrates the robotic simulation, camera data and wireless coverage.

REFERENCES

- [1] A. Guerra, F. Guidi, and D. Dardari, "Position and orientation error bound for wideband massive antenna arrays," in *2015 IEEE International Conference on Communication Workshop (ICCW)*. IEEE, 2015, pp. 853–858.
- [2] A. Shahmansoori, G. E. Garcia, G. Destino, G. Seco-Granados, and H. Wymeersch, "5g position and orientation estimation through millimeter wave mimo," in *2015 IEEE Globecom Workshops (GC Wkshps)*. IEEE, 2015, pp. 1–6.
- [3] F. Guidi, A. Guerra, and D. Dardari, "Millimeter-wave massive arrays for indoor slam," in *2014 IEEE International Conference on Communications Workshops (ICC)*. IEEE, 2014, pp. 114–120.
- [4] 3GPP Technical Report 38.885, "Study on NR positioning support (Release 16)," Mar. 2019.
- [5] 3GPP Technical Report 38.857, "Study on NR positioning enhancements (Release 17)," Mar. 2021.
- [6] 3GPP Technical Report 21.916, "Release description; Release 16 (Release 16)," Jun. 2021.
- [7] R. Keating, M. Säily, J. Hulkkonen, and J. Karjalainen, "Overview of positioning in 5G new radio," in *2019 16th International Symposium on Wireless Communication Systems (ISWCS)*. IEEE, 2019, pp. 320–324.
- [8] S. Dwivedi, R. Shreevastav, F. Munier, J. Nygren, I. Siomina, Y. Lyazidi, D. Shrestha, G. Lindmark, P. Ernström, E. Stare *et al.*, "Positioning in 5G networks," *arXiv preprint arXiv:2102.03361*, 2021.
- [9] L. Zwirello, T. Schipper, M. Harter, and T. Zwick, "Uwb localization system for indoor applications: concept, realization and analysis," *Journal of Electrical and Computer Engineering*, vol. 2012, 2012.
- [10] Y. Zhang, A. K. Brown, W. Q. Malik, and D. J. Edwards, "High resolution 3-d angle of arrival determination for indoor uwb multipath propagation," *IEEE Transactions on Wireless Communications*, vol. 7, no. 8, pp. 3047–3055, 2008.
- [11] D. S. Chaplot, D. Gandhi, S. Gupta, A. Gupta, and R. Salakhutdinov, "Learning to explore using active neural SLAM," *arXiv preprint arXiv:2004.05155*, 2020.
- [12] C. Slezak, V. Semkin, S. Andreev, Y. Koucheryavy, and S. Rangan, "Empirical effects of dynamic human-body blockage in 60 GHz communications," *IEEE Communications Magazine*, vol. 56, no. 12, pp. 60–66, 2018.
- [13] T. S. Rappaport, R. W. Heath Jr., R. C. Daniels, and J. N. Murdock, *Millimeter Wave Wireless Communications*. Pearson Education, 2014.
- [14] I. Guvenc, C.-C. Chong, and F. Watanabe, "Nlos identification and mitigation for uwb localization systems," in *2007 IEEE Wireless Communications and Networking Conference*. IEEE, 2007, pp. 1571–1576.
- [15] S. Venkatesh and R. Buehrer, "Non-line-of-sight identification in ultra-wideband systems based on received signal statistics," *IET Microwaves, Antennas & Propagation*, vol. 1, no. 6, pp. 1120–1130, 2007.
- [16] J. Khodjaev, Y. Park, and A. S. Malik, "Survey of nlos identification and error mitigation problems in uwb-based positioning algorithms for dense environments," *annals of telecommunications-annales des télécommunications*, vol. 65, no. 5, pp. 301–311, 2010.
- [17] D. Wang, M. Fattouche, and X. Zhan, "Pursuance of mm-level accuracy: Ranging and positioning in mmwave systems," *IEEE Systems Journal*, vol. 13, no. 2, pp. 1169–1180, 2018.
- [18] Y. Lu, M. Koivisto, J. Talvitie, M. Valkama, and E. S. Lohan, "Positioning-aided 3D beamforming for enhanced communications in mmWave mobile networks," *IEEE Access*, vol. 8, pp. 55 513–55 525, 2020.
- [19] H. Kim, H. Wymeersch, N. Garcia, G. Seco-Granados, and S. Kim, "5G mmWave vehicular tracking," in *2018 52nd Asilomar Conference on Signals, Systems, and Computers*. IEEE, 2018, pp. 541–547.
- [20] Z. Zhou, J. Fang, L. Yang, H. Li, Z. Chen, and R. S. Blum, "Low-rank tensor decomposition-aided channel estimation for millimeter wave MIMO-OFDM systems," *IEEE Journal on Selected Areas in Communications*, vol. 35, no. 7, pp. 1524–1538, 2017.
- [21] F. Wen, N. Garcia, J. Kulmer, K. Witrissal, and H. Wymeersch, "Tensor decomposition based beamspace ESPRIT for millimeter wave MIMO channel estimation," in *2018 IEEE Global Communications Conference (GLOBECOM)*. IEEE, 2018, pp. 1–7.
- [22] V. Raghavan, L. Akhoondzadeh-Asl, V. Podshivalov, J. Hulten, M. A. Tassoudji, O. H. Koymen, A. Sampath, and J. Li, "Statistical blockage modeling and robustness of beamforming in millimeter-wave systems," *IEEE Transactions on Microwave Theory and Techniques*, vol. 67, no. 7, pp. 3010–3024, 2019.
- [23] W. Xia, V. Semkin, M. Mezzavilla, G. Loianno, and S. Rangan, "Multi-array designs for mmwave and sub-thz communication to uavs," in *2020 IEEE 21st International Workshop on Signal Processing Advances in Wireless Communications (SPAWC)*. IEEE, 2020, pp. 1–5.
- [24] A. Guerra, F. Guidi, and D. Dardari, "Single-anchor localization and orientation performance limits using massive arrays: Mimo vs. beamforming," *IEEE Transactions on Wireless Communications*, vol. 17, no. 8, pp. 5241–5255, 2018.
- [25] C. Huang, A. F. Molisch, R. He, R. Wang, P. Tang, B. Ai, and Z. Zhong, "Machine learning-enabled los/nlos identification for mimo systems in dynamic environments," *IEEE Transactions on Wireless Communications*, vol. 19, no. 6, pp. 3643–3657, 2020.
- [26] R. W. Heath, N. Gonzalez-Prelcic, S. Rangan, W. Roh, and A. M. Sayeed, "An overview of signal processing techniques for millimeter wave MIMO systems," *IEEE journal of selected topics in signal processing*, vol. 10, no. 3, pp. 436–453, 2016.
- [27] F. Xia, A. R. Zamir, Z. He, A. Sax, J. Malik, and S. Savarese, "Gibson env: Real-world perception for embodied agents," in *Proceedings of the IEEE Conference on Computer Vision and Pattern Recognition*, 2018, pp. 9068–9079.
- [28] M. Savva, A. Kadian, O. Maksymets, Y. Zhao, E. Wijmans, B. Jain, J. Straub, J. Liu, V. Koltun, J. Malik *et al.*, "Habitat: A platform for embodied AI research," in *Proceedings of the IEEE/CVF International Conference on Computer Vision*, 2019, pp. 9339–9347.
- [29] "Remcom," available on-line at <https://www.remcom.com/>.
- [30] M. Yin, "mmwRobotNav git hub repository," available on-line at <https://github.com/nyu-wireless/mmwRobotNav>.
- [31] R. W. Heath Jr. and A. Lozano, *Foundations of MIMO Communication*. Cambridge University Press, 2018.
- [32] D. F. Kelley and W. L. Stutzman, "Array antenna pattern modeling methods that include mutual coupling effects," *IEEE Transactions on antennas and propagation*, vol. 41, no. 12, pp. 1625–1632, 1993.
- [33] J. Song, J. Choi, and D. J. Love, "Codebook design for hybrid beamforming in millimeter wave systems," in *2015 IEEE International Conference on Communications (ICC)*. IEEE, 2015, pp. 1298–1303.
- [34] 3GPP Technical Report 38.901, "Study on channel model for frequencies from 0.5 to 100 GHz (Release 16)," Dec. 2019.
- [35] L. Grasedyck, D. Kressner, and C. Tobler, "A literature survey of low-rank tensor approximation techniques," *GAMM-Mitteilungen*, vol. 36, no. 1, pp. 53–78, 2013.
- [36] M. Giordani, M. Polese, A. Roy, D. Castor, and M. Zorzi, "A Tutorial on Beam Management for 3GPP NR at mmWave Frequencies," *IEEE Communications Surveys & Tutorials*, vol. 21, no. 1, pp. 173–196, 2018.
- [37] T. Yu, D. Quillen, Z. He, R. Julian, K. Hausman, C. Finn, and S. Levine, "Meta-world: A benchmark and evaluation for multi-task and meta reinforcement learning," in *Conference on Robot Learning*. PMLR, 2020, pp. 1094–1100.
- [38] F. Xia, W. B. Shen, C. Li, P. Kasimbeg, M. E. Tchampi, A. Toshev, R. Martín-Martín, and S. Savarese, "Interactive gibson benchmark: A benchmark for interactive navigation in cluttered environments," *IEEE Robotics and Automation Letters*, vol. 5, no. 2, pp. 713–720, 2020.
- [39] A. Taha, Q. Qu, S. Alex, P. Wang, W. L. Abbott, and A. Alkhateeb, "Millimeter wave mimo-based depth maps for wireless virtual and augmented reality," *IEEE Access*, vol. 9, pp. 48 341–48 363, 2021.
- [40] W. Khawaja, O. Ozdemir, and I. Guvenc, "UAV Air-to-Ground Channel Characterization for mmWave Systems," in *Proc. IEEE VTC-Fall*, 2017.
- [41] W. Xia, S. Rangan, M. Mezzavilla, A. Lozano, C. Geraci, V. Semkin, and G. Loianno, "Generative neural network channel modeling for millimeter-wave uav communication," *arXiv preprint arXiv:2012.09133*, 2020.
- [42] M. Savva, A. Kadian, O. Maksymets, Y. Zhao, E. Wijmans, B. Jain, J. Straub, J. Liu, V. Koltun, J. Malik, D. Parikh, and D. Batra, "Habitat: A Platform for Embodied AI Research," in *Proceedings of the IEEE/CVF International Conference on Computer Vision (ICCV)*, 2019.
- [43] A. Szot, A. Clegg, E. Undersander, E. Wijmans, Y. Zhao, J. Turner, N. Maestre, M. Mukadam, D. Chaplot, O. Maksymets, A. Gokaslan, V. Vondrus, S. Dharur, F. Meier, W. Galuba, A. Chang, Z. Kira, V. Koltun, J. Malik, M. Savva, and D. Batra, "Habitat 2.0: Training home assistants to rearrange their habitat," *arXiv preprint arXiv:2106.14405*, 2021.
- [44] E. Dahlman, S. Parkvall, and J. Skold, *5G NR: The next generation wireless access technology*. Academic Press, 2020.
- [45] X. Gu, A. Paidimarri, B. Sadhu, C. Baks, S. Lukashov, M. Yeck, Y. Kwark, T. Chen, G. Zussman, I. Seskar *et al.*, "Development of a compact 28-GHz software-defined phased array for a city-scale wireless research testbed," in *Proc. IEEE Int. Microw. Symp. (IMS)*, 2021, pp. 1885–1889.

- [46] V. Raghavan, M.-L. Chi, M. A. Tassoudji, O. H. Koymen, and J. Li, "Antenna placement and performance tradeoffs with hand blockage in millimeter wave systems," *IEEE Transactions on Communications*, vol. 67, no. 4, pp. 3082–3096, 2019.
- [47] R. Garg and A. S. Natarajan, "A 28-ghz low-power phased-array receiver front-end with 360° rtps phase shift range," *IEEE Transactions on Microwave Theory and Techniques*, vol. 65, no. 11, pp. 4703–4714, 2017.
- [48] V. Nair and G. E. Hinton, "Rectified linear units improve restricted boltzmann machines," in *Icml*, 2010.
- [49] D. P. Kingma and J. Ba, "Adam: A method for stochastic optimization," *arXiv preprint arXiv:1412.6980*, 2014.
- [50] J. Palacios, G. Bielsa, P. Casari, and J. Widmer, "Communication-driven localization and mapping for millimeter wave networks," in *IEEE INFOCOM 2018-IEEE Conference on Computer Communications*. IEEE, 2018, pp. 2402–2410.